AGU PUBLICATIONS

JGR

Journal of Geophysical Research: Solid Earth

RESEARCH ARTICLE
10.1002/2016JB013228

Key Points:
- Ridge to trench 2-D velocity model of the Juan De Fuca plate
- The mantle of the subducting JdF plate is dry to very mildly hydrated
- Propagator wakes are zones of enhanced hydration that may affect subduction zone processes

Supporting Information:
- Supporting Information S1

Correspondence to:
G. Horning,
horning@mit.edu

Citation:
Horning, G., J. P. Canales, S. M. Carbotte, S. Han, H. Carton, M. R. Nedimović, and P. E. van Keken (2016), A 2-D tomographic model of the Juan de Fuca plate from accretion at axial seamount to subduction at the Cascadia margin from an active source ocean bottom seismometer survey, *J. Geophys. Res. Solid Earth*, *121*, 5859–5879, doi:10.1002/2016JB013228.

Received 2 JUN 2016
Accepted 19 JUL 2016
Accepted article online 22 JUL 2016
Published online 14 AUG 2016

A 2-D tomographic model of the Juan de Fuca plate from accretion at axial seamount to subduction at the Cascadia margin from an active source ocean bottom seismometer survey

G. Horning[1,2], J. P. Canales[2], S. M. Carbotte[3], S. Han[3,4], H. Carton[3,5], M. R. Nedimović[3,6], and P. E. van Keken[7]

[1]Massachusetts Institute of Technology/Woods Hole Oceanographic Institution Joint Program in Oceanography/Applied Ocean Science and Engineering, Woods Hole, Massachusetts, USA, [2]Department of Geology and Geophysics, Woods Hole Oceanographic Institution, Woods Hole, Massachusetts, USA, [3]Lamont-Doherty Earth Observatory, Columbia University, Palisades, New York, USA, [4]Now at Institute for Geophysics, University of Texas at Austin, Austin, Texas, USA, [5]Now at Institut de Physique du Globe de Paris, Paris, France, [6]Department of Earth Sciences, Dalhousie University, Halifax, Nova Scotia, Canada, [7]Department of Terrestrial Magnetism, Carnegie Institute for Science, Washington, District of Columbia, USA

Abstract We report results from a wide-angle controlled source seismic experiment across the Juan de Fuca plate designed to investigate the evolution of the plate from accretion at the Juan de Fuca ridge to subduction at the Cascadia margin. A two-dimensional velocity model of the crust and upper mantle is derived from a joint reflection-refraction traveltime inversion. To interpret our tomography results, we first generate a plausible baseline velocity model, assuming a plate cooling model and realistic oceanic lithologies. We then use an effective medium theory to infer from our tomography results the extent of porosity, alteration, and water content that would be required to explain the departure from the baseline model. In crust of ages >1 Ma and away from propagator wakes and regions of faulting due to plate bending, we obtain estimates of upper crustal hydration of 0.5–2.1 wt % and find mostly dry lower crust and upper mantle. In sections of the crust affected by propagator wakes we find upper estimates of upper crustal, lower crustal, and upper mantle hydration of 3.1, 0.8, and 1.8 wt %, respectively. At the Cascadia deformation front, we find that the amount of water stored at uppermost mantle levels in the downgoing JdF plate is very limited (<0.3 wt %), with most of the water carried into the subduction zone being stored in the oceanic crust.

1. Introduction

Water incorporated into oceanic lithosphere prior to and with onset of subduction is the primary source of water transfer within the subduction zone [*Rüpke et al*., 2004]. As the plate descends, metamorphic dehydration reactions resulting from increasing pressure and temperature [*van Keken et al*., 2011] provide a mechanism for significant delivery of water at depth [*Kawakatsu and Watada*, 2007]. Free water and the presence of hydrous phases in the subducting slab both affect a number of subduction zone processes such as [*Hacker et al*., 2003] the following.

1. The presence of serpentine decreases the shear strength of peridotite [*Escartín et al*., 2001], affecting the rheology of the mantle wedge [*Billen and Gurnis*, 2001].
2. Episodic tremor and slip events have been linked to fluid overpressures at and above the plate interface [*Obara*, 2002; *Rogers and Dragert*, 2003].
3. Dehydration embrittlement of the subducting slab may be responsible for intraslab seismicity [e.g., *Hacker et al*., 2003].
4. By decreasing the solidus of the mantle, water plays an important role in the formation of magmas and active volcanic arcs [*Tatsumi*, 1989].

The total water content of an incoming plate can be considered as the sum of the free water in pore spaces in the sedimentary cover and highly porous upper crust (which is mostly lost in the shallow forearc region), chemically bound water in sediment clay minerals, chemically bound water in the upper and lower crust resulting from the precipitation of secondary hydrous alteration products, free water in fault zones, and bound water of hydrous minerals in the uppermost mantle resulting from serpentinization of peridotite. On the basis

of modeling of global subduction zones, *Hacker* [2008] concludes that oceanic mantle, which is the least well constrained, is the primary source of water subducted to postarc depths.

Hydration of oceanic crust begins in the near-axis region where fluid circulation along joints and cracks is driven by strong thermal gradients associated with crustal formation [*Elderfield and Schulz*, 1996]. At the axis both high-temperature focused flow and low-temperature diffuse drive hydration of the upper and perhaps middle crust through alteration of basaltic rocks and mineral precipitation in the pore space of the crust [*Alt et al*., 1986]. As the plate ages, hydration continues driven by low-temperature circulation associated with conductive plate cooling [*Elderfield and Schulz*, 1996]. Sediment blanketing of the oceanic crust and precipitation of hydrous phases in cracks and joints limit the open exchange of seawater within the crust, thus reducing the potential of the plate to incorporate more water as it ages. The "sealing age" of the plate is therefore dependent on both spreading and sedimentation rates [e.g., *Nedimović et al*., 2008].

Geochemical, petrological, and geophysical constraints suggest that the lower oceanic crust is dry prior to hydrothermal alteration [e.g., *Hirth et al.,* 1998, and references therein]. The onset and extent of lower crustal hydrothermal alteration depends on the axial thermal structure and the distribution of permeable pathways and is a topic of ongoing debate. Cores drilled in exposed lower crustal rocks off the East Pacific Rise (EPR) reveal alteration along cracks through the precipitation of hydrous phases within 1 Myr of crustal accretion [*Lécuyer and Reynard*, 1996].

As the plate approaches a subduction zone, a secondary phase of hydration may occur because plate bending-related faulting creates a pervasive tectonic fabric throughout the crust and upper mantle [*Peacock*, 2001; *Ranero et al*., 2003]. Stresses created by the bending of the subducting slab result in subhydrostatic pressure gradients localized along faults which can penetrate tens of kilometers below the Moho, pumping fluids downward from the saturated upper crust to the dry lower crust and upper mantle [*Faccenda et al*., 2009].

The faulting of the oceanic lithosphere as it enters a subduction zone may lead to decreased seismic velocities through fracturing and increased porosity as well as subsequent hydration due to fluids migrating along those cracks. Low seismic velocities near the Chile and Nicaragua trenches have been used to estimate the extent of hydration of the incoming mantle [e.g., *Contreras-Reyes et al*., 2007; *Ivandic et al*., 2008; *van Avendonk et al*., 2011]. Offshore central Nicaragua, a velocity decrease of 5–7% in the uppermost 3–4 km of the mantle was found seaward of the outer trench rise, indicating increasing crack density and/or systematic serpentinization of 12–17% (1.55–2.17 wt % water) [*Ivandic et al*., 2008]. On a trench-parallel (15–20 km from the trench) profile over the Cocos plate, *van Avendonk et al.* [2011] estimate ~1 wt % water content in the lower crust offshore Nicaragua and uppermost mantle serpentinization of up to 30% (3.5 wt % water) offshore central and northwestern Nicaragua and 8–17% (1–2 wt % water) in the southeast. South-central Chile similarly displays a decrease in upper mantle velocities in the trench and outer rise area. There, the thick sedimentary cover is thought to impede hydration which is reflected in an upper bound estimate of 9% serpentinization in the uppermost 2 km of the mantle [*Contreras-Reyes et al*., 2007]. In all of these cases the decrease in upper mantle seismic velocity coincides with the onset of bending-related faults observed in seafloor bathymetry.

At the Cascadia subduction zone, the state of hydration of the Juan de Fuca (JdF) plate is of particular interest because little hydration of the downgoing plate is expected based on its young age and presumably warm state [e.g., *Hyndman and Wang*, 1993]. However, numerous observations consistent with slab dehydration suggest significant hydration of the downgoing plate [e.g., *Audet et al*., 2009; *Bostock et al*., 2002; *Hacker et al*., 2003; *Kao et al*., 2005; *Preston et al*., 2003; *Rogers and Dragert*, 2003; *Walowski et al*., 2015]. Prior studies within the interior of the JdF plate provide evidence for hydration of the upper crust associated with ridge flank hydrothermal circulation and spatially correlated with local zones of ridge propagation [*McClymont and Clowes*, 2005; *Nedimović et al*., 2009, 2008; *Newman et al*., 2011] but the full extent of when and how water is incorporated into the lithosphere during the evolution of the JdF plate, and how water is distributed at depth within the plate prior to subduction remains unknown. To address this important question, we conducted in 2012 an active source seismic study to characterize crustal and shallow mantle velocities and distribution of faulting along two ridge-perpendicular transects spanning the full width of the JdF plate and a trench-parallel line to characterize along-margin variations in the architecture and velocity structure of the downgoing plate [*Carbotte et al*., 2014; *Han et al*., 2016]. Here we present a *P* wave seismic

tomography model of the sediments, crust, and uppermost mantle along one of the plate transects extending from 0.7 Ma crust near Axial volcano to the Cascadia margin offshore central Oregon. We use the evolution of seismic velocities from the ridge to the deformation front as indicators of alteration and porosity changes at different levels and provide an estimate of the water content of the plate under different plausible mineralogical assumptions. This work, based on wide-angle ocean bottom seismometer (OBS) data, complements that of *Han et al.* [2016], who reported the results from analysis of multichannel seismic (MCS) data that document the distribution of faulting along both plate transects. Results from the remaining transects will be published elsewhere.

2. Tectonic Setting

2.1. The Juan de Fuca Ridge

The JdF plate is formed at the intermediate spreading (25–33 mm/yr half rate [*Wilson*, 1993]) JdF Ridge (JdFR). The JdFR is split into seven primary segments: Cleft, Vance, Axial, Coaxial, Northern Symmetric, Endeavor, and Middle/West Valley (Figure 1). The JdFR has a northwesterly absolute motion that has recently (0.5 Ma) brought it into contact with the Cobb hot spot [*Karsten and Delaney*, 1989], currently located beneath Axial seamount. In addition to Axial seamount, a broad plateau centered on the Cleft segment associated with 0.7–1.0 km thicker crust is thought to be the result of increased crustal production in the last 0.5 Ma related to the Cobb hot spot combined with a preferential southward channeling of melt supply [*Carbotte et al*., 2008]. Similarly, the Endeavor segment has a large plateau related to increased crustal thickness as a result of interaction with the Heckle melt anomaly [*Carbotte et al*., 2008]. Morphology of the ridge is characterized by axial summit grabens created by dike-induced faulting [*Carbotte et al*., 2006] and their large sensitivity to small fluctuations in magma supply at this spreading rate [*Canales et al*., 2005]. The depth to the seismically imaged axial melt lenses generally increases to the north from 2.1 km at Cleft to 2.6 km at Endeavor [*Carbotte et al*., 2006]. An exception to this trend is Axial seamount, where the depth to the top of the magma reservoir varies between 1.1 and 2.3 km [*Arnulf et al*., 2014].

2.2. The Juan de Fuca Plate Interior

The JdF plate is crosscut by a number of "pseudofaults" or propagator wakes, which result from the growth or "propagation" of one spreading ridge segment across a small ridge offset into preexisting crust formed at an adjacent "dying" ridge segment [*Wilson*, 1988] (Figure 1). As a result of propagation, crust transferred from one plate to another results in plate age reversals along the spreading direction [*Hey et al*., 1980]. Propagation also rotates and shears the crust within its wake [*Hey et al*., 1980] resulting in higher porosity and alteration, as has been inferred from seismic studies on the flanks of the EPR [e.g., *Canales et al*., 2003] and JdFR [e.g., *McClymont and Clowes*, 2005; *Nedimović et al*., 2008]. As a result of this shearing and alteration, propagator wakes are potential areas of enhanced fluid flow [*Nedimović et al*., 2008]. On the basis of velocity-density relationships and gravity anomalies, *McClymont and Clowes* [2005] further propose that propagator wakes are locations of partial upper mantle serpentinization. Nine major events of ridge propagation at the JdFR have occurred during the last 18 Ma [*Wilson*, 1988; *Wilson*, 1993]. Using gravity and seismic data *Marjanović et al.* [2011] find thinner and/or more dense crust within these propagator wakes. Additionally, they find the presence of 10–20 km wide zones of thicker crust located on the young crust side of the propagators at distances up to 10 km from the edge of the wake. Within these wide zones of thicker crust *Nedimović et al.* [2005] imaged bright subhorizontal to shallowly ridgeward dipping seismic reflectors in the mantle which they interpreted as frozen subcrustal magma chambers related to the propagation of the ridge axis.

In the interior of the plate, hydration of the upper crust is inferred from observations of increasing *P* wave velocities within seismic layer 2A and 2B with increasing crustal age and sediment cover [*Nedimović et al*., 2008; *Newman et al*., 2011]. The thickness of the sedimentary cover varies in the N-S direction across the JdF plate with full burial of the oceanic crust at younger ages in the north decreasing strongly to the south. Compared to regions with limited sedimentary cover, larger increases in velocities at young crustal ages are found in regions of full sediment burial near the ridge axis [*Nedimović et al*., 2008]. This is a consequence of fluid circulation in a high-permeability JdF upper crust [*Davis et al*., 1997] that results in alteration and mineral precipitation increasing with sedimentary cover [*Hunter et al*., 1999; *Nedimović et al*., 2008]. The documented spatial variations in crustal velocities therefore imply greater extents of hydration in the upper crust in the north than farther south along the plate.

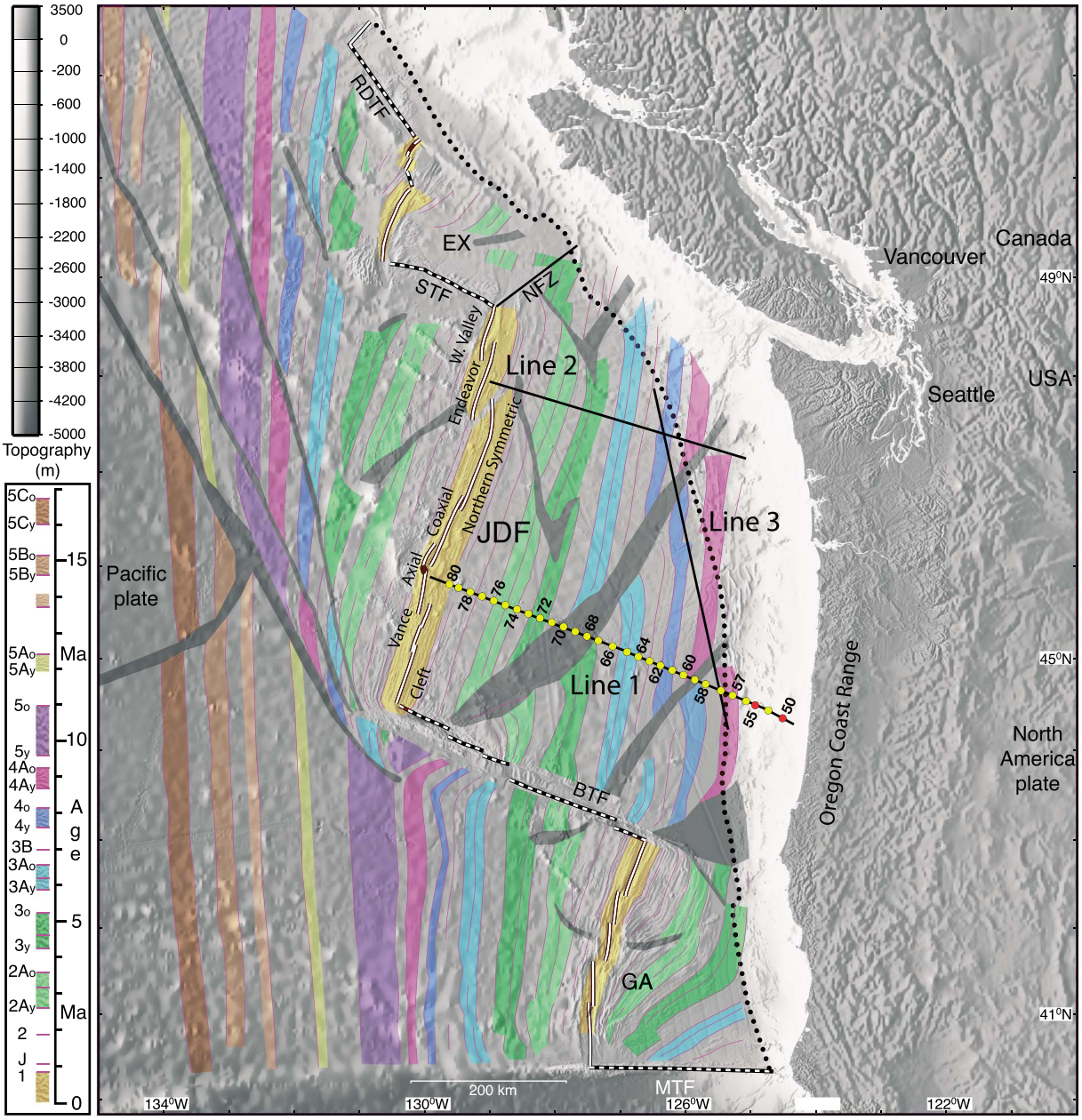

Figure 1. Location of the Juan de Fuca ridge-to-trench seismic profiles Lines 1, 2, and 3. OBS positions for Line 1 are marked with yellow circles (some of them numbered; red for instruments that did not return data or were not used). Color bands correspond to magnetic isochrones from *Wilson* [2002]. Dark gray shaded regions correspond to propagator wakes. Dotted black line is the Cascadia deformation front. Ridge axis is shown in yellow lines, and fracture zones in black-white lines. JDF, Juan de Fuca plate; EX, Explorer plate; GA, Gorda deformation zone; RDTF, Revere-Dellwood transform fault; STF, Sovanco transform fault; NF, Nootka fault zone; BTF, Blanco transform fault; and MTF, Mendocino transform fault. Figure is modified from *Nedimović et al.* [2009].

2.3. The Cascadia Subduction Margin

The structure of the Cascadia forearc region varies significantly along strike in response to changes in thickness (or absence) of the accreted oceanic Siletz terrane [*Tréhu et al.*, 1994]. Thickness of the terrane reaches a maximum value of 25–35 km beneath the Oregon Coast Range. This area is considered to be the region of greatest strength of the forearc crust which is reflected in low rates of forearc seismicity, the narrowest subduction complex width, and a region of smaller but more mafic arc volcanic activity [*Tréhu et al.*, 1994]. To the north of the Oregon Coast Range, the Siletz terrane thickness decreases with a minimum value of 6 km offshore Vancouver Island. South of the Oregon Coast Range the Siletz terrane is absent, with the forearc

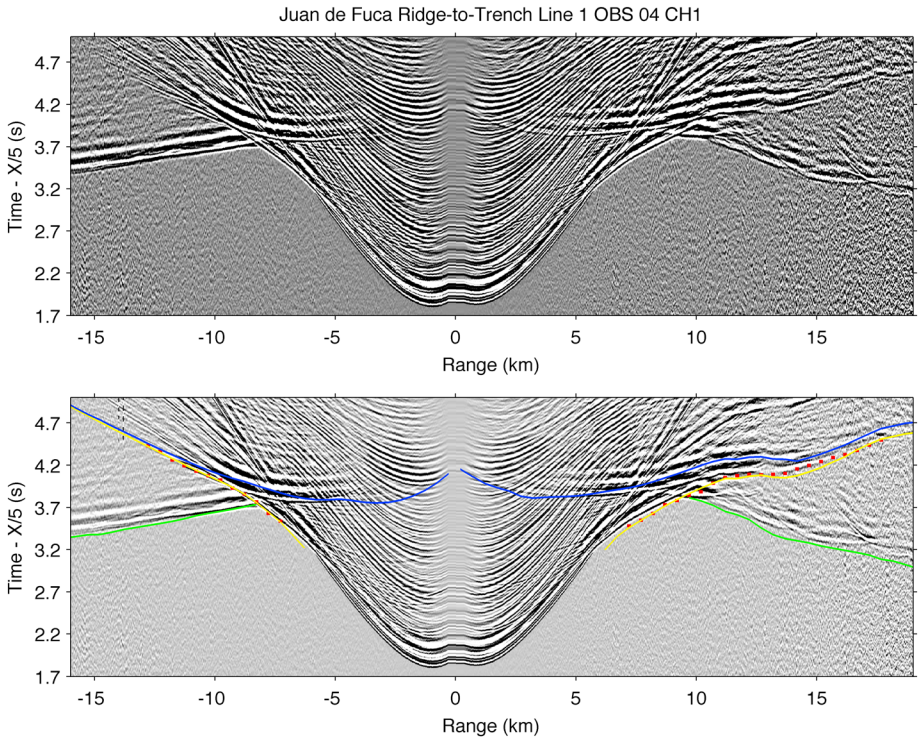

Figure 2. (top) OBS data from instrument 57 with intershot spacing of 37.5 m. Clear sediment refraction (*Ps*) and subbasement crustal refraction (*Pg*) arrivals are present. (bottom) Picked arrival times for *Ps* (red) are plotted with predicted arrival times from forward modeling of final model in yellow, light green, and dark blue for *Ps*, *Pg*, and basement reflection (*PbP*), respectively.

instead mostly supported by the Klamath block [*McCrory and Wilson*, 2013]. The regions of thin or absent Siletz terrane are areas of increased forearc seismicity, increased subduction complex width, and more silicic and voluminous volcanic activity [*Tréhu et al*., 1994]. The seismic investigation of *Gerdom et al.* [2000] of the internal structure of the Cascadia accretionary prism offshore Oregon found that the dip of the subducting Juan de Fuca plate increases from 1.5° to 6.5° to 16° as it moves from the trench to beneath the accretionary complex to east of the coast. Additionally, *Gerdom et al.* [2000] find that the base of the Siletz terrane seems to be in contact with the subducting oceanic crust, which would suggest that no large volume of sediment is subducted to greater depth offshore Oregon.

Hydration of the lower crust and upper mantle just seaward of the deformation front is expected to be limited due to the young age (5–9 Ma [*Wilson*, 1988; *Wilson*, 2002], Figure 1) and warm thermal regime of the JdF plate [*Hyndman and Wang*, 1993; *Wada and Wang*, 2009]. Previous reflection studies revealed pervasive faulting in the sedimentary section blanketing the Juan de Fuca plate starting ~200 km west of the deformation front, but whether there is any significant crustal hydration associated with this faulting was unknown [*Nedimović et al*., 2009]. The new seismic reflection images of *Han et al.* [2016] reveal faults closer to the deformation front that cut the crust and reach down to and beneath Moho levels offshore Oregon. Offshore Washington, faults are slightly steeper, dominantly dip seaward, and do not extend into the lower crust or upper mantle. Based on these differences in the extent of crustal/mantle faulting near the deformation front, *Han et al.* [2016] infer that the oceanic plate offshore Oregon has a higher potential for crustal alteration and mantle serpentinization than offshore Washington.

Within the Cascadia subduction zone, numerous observations suggest significant hydration of the lower crust and upper mantle of the downgoing JdF plate. Episodic nonvolcanic tremors [*Rogers and Dragert*, 2003] associated with slow slip along the subduction interface [*Dragert et al*., 2001] are abundant in the Cascadia subduction zone, and their occurrence is thought to be facilitated by slab-derived fluids based on the location of the tremor in close proximity to strong seismic reflectors above the plate interface [*Kao et al*., 2005]. Intraslab seismicity located at intermediate depths is generally thought to arise from dehydration

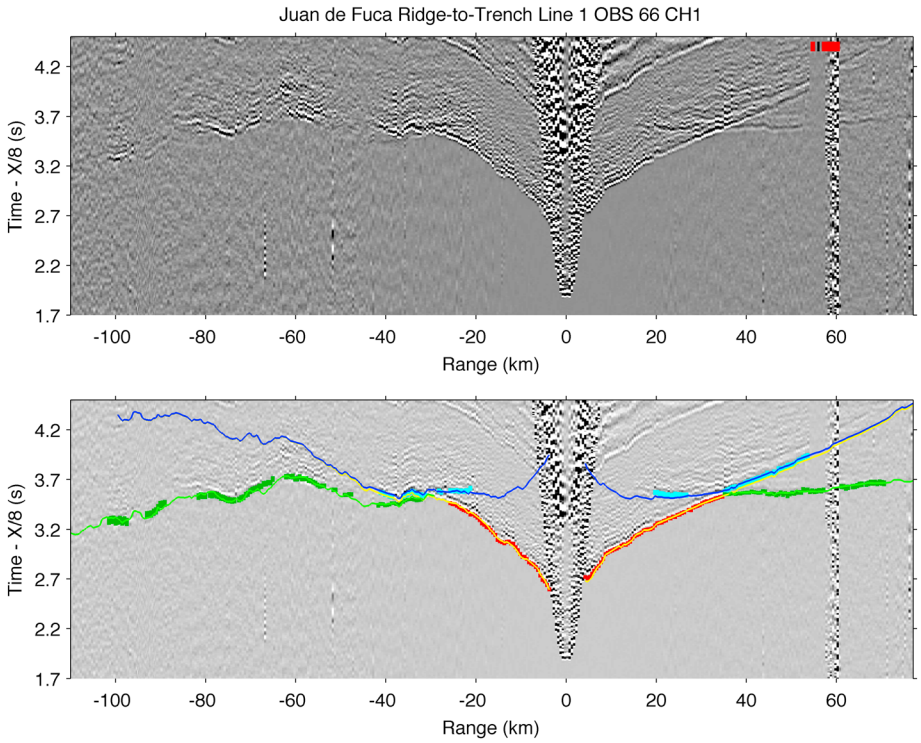

Figure 3. (top) OBS data from instrument 66 with intershot spacing of 500 m. Clear *Pg*, *PmP*, and *Pn* arrivals are present. Data gaps from mitigation shooting (red bars) or skipped shots (black bar) are indicated for the ranges affected. (bottom) Picked arrival times for *Pg* (red), *PmP* (light blue), and *Pn* (dark green) are plotted with predicted arrival times from forward modeling of final model in yellow, light green, and dark blue for *Pg*, *PmP*, and *Pn*, respectively.

reactions [*Kao et al*., 2008; *Preston et al*., 2003]. Reflection banding is also present above the megathrust and is likely related to fluids given the high electrical conductivity associated with this zone [*Nedimović et al*., 2003]. Low shear wave velocities in the forearc mantle from teleseismic waveform inversions suggest that the forearc region is highly hydrated and serpentinized due to fluids released from the slab as the subducting crust undergoes eclogitization [*Bostock et al*., 2002].

3. Data Acquisition

In June–July 2012 a two-ship seismic experiment was conducted using the R/V *Oceanus* (cruise OC1206A) and the R/V *Marcus G. Langseth* (cruise MGL1211) with the main objective of understanding the state of hydration of the JdF plate from ridge to trench as well as along strike of the subduction zone to inform the interpretation of along-strike variation in subduction zone processes. Active source 2-D MCS reflection profiles were collected by the R/V *Marcus G. Langseth* along three main lines (Figure 1): two plate transects from the JdFR to the Cascadia margin (Line 1, from Axial volcano to offshore central Oregon, and Line 2 from Endeavor segment to offshore central Washington) and a margin-parallel profile (Line 3) connecting the plate transects and located ~10 km seaward from the Cascadia deformation front. MCS acquisition parameters are given in *Han et al.* [2016]. Wide-angle reflection/refraction data were collected along the same profiles, which were instrumented with short-period OBSs from the OBSIP instrument pool (obsip.org). OBS deployments and recoveries were conducted from RV *Oceanus*. OBS seafloor locations were determined by shipboard acoustic surveying or by direct wave arrival traveltime relocation. OBS sample rate was 200 Hz for four channels (three-channel seismometer and hydrophone). The OBSs recorded air gun shots from the Langseth's 6600 cu in. air gun array, which was triggered every 37.5 m for MCS profiling and every 500 m for the wide-angle survey. The highly dense spatial data sampling of the MCS shots allows for detailed identification of near-offset, shallow arrivals (i.e., sediments and upper crust) in the OBS records (Figure 2), while OBS recordings of the large shot spacing result in records with high signal-to-noise ratio at large offsets appropriate for identifying crustal and mantle arrivals (Figure 3).

Table 1. Data Fit Statistics[a]

Stage	Phase	N	λ	L_H (km)	L_Z (km)	RMS	χ^2
I	*Ps*	1388	15	3	0.3	17	0.25
II	*Pg*	2414	15	3	0.3	17	0.76
II	*PmP*	2695	15	6	0.3	30	1.5
III	*Pn*	2602	150	6	1	25	0.97

[a] N is number of picks. λ is a smoothing weight; L_H and L_Z are horizontal and vertical correlation lengths, respectively; and χ^2 is the RMS normalized by the pick uncertainty.

Here we report observations and results obtained along Line 1, which included 29 OBSs at 16 km instrument spacing (Figure 1). Our analysis of Line 1 data includes minimal processing of the MCS data to image igneous basement and measure sediment thickness and detailed traveltime tomography of the OBS data to determine the *P* wave velocity structure of the sediments, crust, and upper mantle. An in-depth analysis of Line 1 and 2 MCS data is presented by *Han et al.* [2016]; OBS results from the other profiles will be presented elsewhere. Source data used for this study are archived through IRIS (OBS data [*Canales and Carbotte*, 2012]) and the MGDS (MCS data [*Carbotte et al.*, 2014]).

4. Data Processing

4.1. MCS Data

For the purposes of this paper we processed the MCS data up to a poststack migrated section, focusing on imaging the igneous basement to be used as a constraint on the tomographic inversions. Imaging crustal and mantle reflectivity from these data is presented in *Han et al.* [2016]. Our processing consisted of (1) common-midpoint (CMP) geometry definition and gathering, (2) stacking velocity analysis, (3) spherical divergence correction, (4) surface-consistent amplitude balancing, (5) 3–60 Hz bandpass filtering, (6) normal-moveout correction, (7) CMP stacking, (8) mute seafloor multiple, and (9) poststack F-K domain time migration. The seafloor-to-basement two-way traveltime along Line 1 was digitized from the migrated image.

4.2. OBS Data

The OBS data were used to derive a *P* wave velocity model based on the arrival times of the following phases: sediment refractions (*Ps*), subbasement crustal refractions (*Pg*), Moho wide-angle reflections (*PmP*), and sub-Moho refractions (*Pn*).

OBS data were filtered between 5 and 20 Hz for phase interpretation and traveltime picking. Predictive deconvolution to minimize reverberations from the source bubble and suppress internal multiples was performed on the OBS records of large shot spacing to improve imaging of the *PmP* triplication. Details of picking for each phase are given in Table 1. Examples of typical OBS records and the corresponding traveltime picks are presented in Figures 2 and 3. Record sections for all the OBS for both large and small shot spacing are included in the supporting information.

5. Velocity Modeling

The 2-D tomographic velocity model inversion and ray tracing was performed using the joint refraction/reflection method Tomo2D [*Korenaga et al.*, 2000]. Tomo2D uses a 2-D starting model and traveltime picks to solve the forward problem and invert for a new velocity model and depth to a floating reflector. The model space is parameterized as a sheared grid of variable spacing, hung from the bathymetric profile. Horizontal node spacing was set to a constant 250 m, while vertical node spacing was set to 100 m for the first 2 km, 200 m to 4 km, 300 m to 7 km, and 500 m to the bottom of the model. Overall dimensions of the model are 2090 nodes along the profile in X direction and 107 nodes in depth or Z direction. Bathymetry along the profile was constructed from multibeam data from the RV *Langseth* EM-122 echosounder. The forward problem is solved using a hybrid of the graph and ray bending methods [*Korenaga et al.*, 2000; *van Avendonk et al.*, 1998]. The inverse problem uses the sparse matrix solver LSQR to solve a regularized linear system with model parameters including *P* wave velocity at each model node and depth to reflector weighted by smoothing and damping parameters [*Korenaga et al.*, 2000]. Trade-off between perturbations in velocity versus reflector depth is controlled by a depth kernel weighting parameter w [*Korenaga et al.*, 2000]. Smoothing is imposed by a parameter λ that controls the relative importance of smoothing constraints with respect to

the data resolution [*Korenaga et al*., 2000]. Damping constraints are also placed on the model to decrease the amplitude of model parameter perturbations when starting with a model with large misfit.

We followed a top down modeling approach, starting with the sedimentary layer, then the crust, and finally the mantle. At each stage, the structure of the overlaying layers obtained from the previous stage was kept fixed during the inversion. This was accomplished by imposing large damping values to model parameters located above a predetermined interface: the basement for the Stage 2 inversions (crust) and the Moho reflector for the Stage 3 inversion (mantle). This strategy ensures that velocity perturbations at each stage occur only below the predetermined interface.

Rather than using a single starting model at each stage, we followed the Monte Carlo approach described in *Korenaga et al.* [2000]. This approach allows estimating the model uncertainty arising from the dependence of inversion results on the initial assumptions. At each stage we computed 100 solutions starting from random initial models (details of models are in the supporting information). Each Monte Carlo solution was obtained after several inversions, starting with a large λ value to obtain a long-wavelength structure and then continued to lower λ values to allow shorter-wavelength perturbations to the model as required by the data. The preferred solution for each stage was then calculated as the average of the 100 Monte Carlo solutions, and the model uncertainty estimate as the standard deviation of the 100 Monte Carlo solutions.

The quality of the data fit was evaluated using the root-mean-square (RMS) value of the difference between the predicted and observed travel times and the χ^2 (RMS misfit normalized by pick error). Data fit convergence was deemed adequate when the χ^2 reached unity. Data fit statistics for the preferred solutions after each inversion stage are given in Table 1.

5.1. Stage 1: Sediments

For simplicity we refer to "sediments" as the layer above the igneous JdF plate oceanic basement everywhere along our model, including the continental shelf east of the deformation front. Thus, our sedimentary layer represents the pelagic and turbiditic sediments west of the deformation front, as well as the accretionary wedge and subducting sediments, and the western edge of the igneous Siletz terrane [*Gerdom et al*., 2000; *Tréhu et al*., 1994] east of the deformation front. We refer to refractions within any of these units collectively as *Ps* arrivals. Only data from 12 instruments (50–65, Figure 1) were used at this stage, as sediments beyond 140 km west of the deformation front are too thin to produce usable *Ps* arrivals in the OBSs.

Using the Monte Carlo approach described above during this first stage resulted, in the following stage, in highly uncertain crustal velocities beneath the continental shelf due to the lack of deep-penetrating *Ps* rays that sample zones of high sedimentary *P* wave velocity and the western edge of the Siletz terrane [*Gerdom et al*., 2000; *Tréhu et al*., 1994]. Therefore, we modeled the sediment layer in two separates parts: one covering the model section seaward from the deformation front using the Monte Carlo approach described above, and a second one covering the landward part of the model in which a single 2-D starting model from *Gerdom et al.* [2000] was used. To compensate for the lack of deep-penetrating *Ps* rays beneath the continental shelf, inversion of the landward part of the model also included vertical-incidence basement traveltimes derived from the MCS data [*Han et al*., 2016], thus increasing the ray coverage in a region of the model with sparse coverage from the OBS data. Both solutions were then merged into a single model and further refined to provide one internally consistent solution to all *P*s traveltimes.

The OBS records of the MCS shots show clear reflections from the basement (*PbP*, Figure 2). Although this information could be used to constrain sediment thickness, we did not include this phase in our modeling because sediment thickness derived from the MCS images is more accurate and has higher lateral resolution. To determine the thickness of the sedimentary cover, the two-way traveltime difference between the seafloor and basement reflectors on the MCS profile was used in conjunction with the velocity model obtained in Stage 1.

The Stage 1 results (shown as part of the final model in Figure 4) have no or very thin sedimentary cover from the seaward end of the profile until ~250 km west of the deformation front where there is a small basin bounded on the east by a narrow (10 km wide) basement high. Sedimentary thickness then begins to gradually increase landward starting at 200 km west of the deformation front and reaching 3.1-3.2 km at the trench. Sediment velocities start at ~1.7 km/s at the seafloor with a vertical gradient of 0.6 s^{-1} through the sediment section. The sedimentary velocity model shows only a small variation from a 1-D reference velocity model.

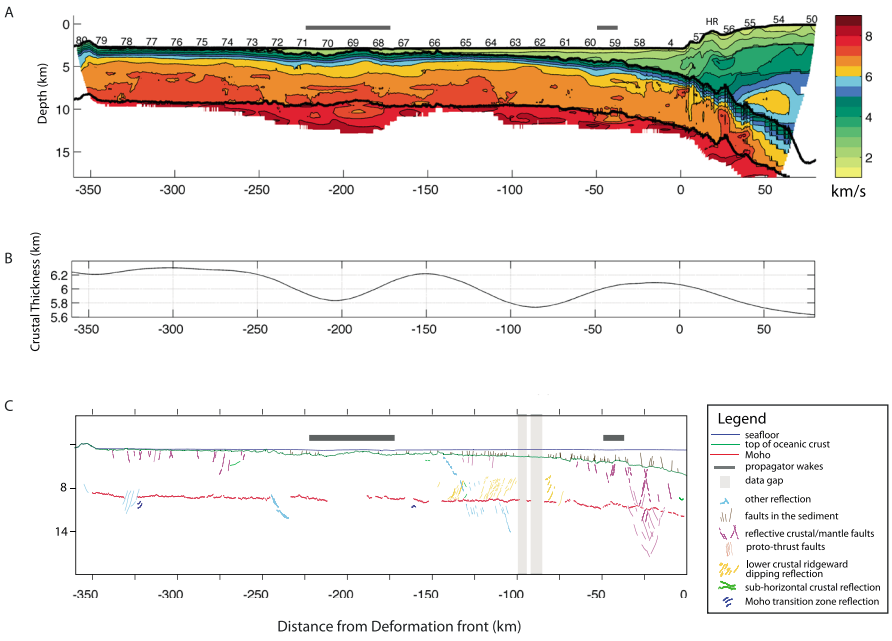

Figure 4. (a) Final 2-D velocity model. Thick gray bars indicate location of propagator wakes. OBS numbers (see Figure 1) are shown at the top. "HR" denotes location of Hydrate Ridge between OBSs 56 and 57. (b) Crustal thickness along line. (c) Interpretation of prestack time migrated multichannel seismic (MCS) images of the Oregon transect from *Han et al.* [2016]. Features are annotated in the legend table. Vertical exaggeration is ~7 times.

Our experimental setup provided ray coverage in the eastern portion of the sedimentary sequence (<140 km west of the deformation front) where the sedimentary thickness is significant (Figure 4a). Due to the expected small lateral variation in sedimentary velocities the extrapolation of the model to the west (>140 km) based on results obtained within areas with ray coverage is justified. Furthermore, due to the decreasing sedimentary thickness to the west any velocity inaccuracy from this extrapolation will result in very small errors in sediment thickness.

5.2. Stage 2: Crust and Moho

A new set of Monte Carlo initial models was constructed using the sedimentary velocity model and basement depth of Stage 1 and randomized 1-D crustal structure (see supporting information) hung beneath the crust-sediment interface. For this stage we used *Pg* and *PmP* arrivals observed in the OBS records of large shot spacing. In order to keep the sedimentary layer structure constant, we imposed a large damping value to grid points above the basement interface. This strategy ensures that any velocity perturbations from the inversion of crustal phases occur in the crustal layer of the model. The trade-off between velocity perturbations within the crust and Moho depth is controlled in the inversion through a depth kernel weighting factor, *w*. A value of 1 representing equal weighting was used. Sensitivity of the results to this parameter was evaluated using a range of larger values of *w*. Generally, increasing *w* leads to larger deviations of the inverted reflector depth from the starting model as well as larger model misfit. Thus, the choice of equal weighting seems appropriate.

The Stage 2 model shows ray coverage from *Pg* and *PmP* phases that extends 350 km west of the deformation front to 40 km east for the full thickness of the crust (Figure 4). Velocities at the top of the crust gradually increase from 3.1 ± 0.1 km/s at 360 km west of the deformation front to 4.3 ± 0.8 km/s beneath the trench. Lower crustal velocities drop from 7.1–7.3 ± 0.15 km/s to 6.9–7.0 ± 0.1 km/s beginning ~100 km west of the deformation front. Crustal thickness along the line has a maximum of 6.3 ± 0.3 km at 300 km from the deformation front. Crustal thickness shows a slight decreasing trend toward the trench reaching 6.1 ± 0.5 km at the trench.

5.3. Stage 3: Mantle

Following a satisfactory inversion for *Pg* and *PmP* ($\chi^2 \sim 1$, Table 1), the mantle phases *Pn* were included in the inversion. A new set of initial models was constructed by using the sedimentary and crustal velocity model of

Stages 1 and 2, and randomized 1-D mantle structure (see supporting information) hung beneath the Moho interface. The sedimentary and crustal structures were held constant by imposing large damping values to model parameters above the Moho interface.

The Stage 3 model has ray coverage in the uppermost mantle with a range of penetration of 0.5 to 4 km below Moho (Figure S1). Velocities in the upper mantle are generally 7.9–8.1 ± 0.1 km/s. Two large low-velocity anomalies are present; one wide zone is located at 170–220 km west of the deformation front and one narrow zone 40–50 km west of the deformation front. These two low-velocity zones have values as low as 6.9 ± 0.4 km/s and are spatially correlated with the location of propagator wakes.

5.4. Monte Carlo Uncertainty Estimation

A measure of the uncertainty of the models arising from the dependence of inversion results on the initial assumptions was estimated by calculating the standard deviation of all the Monte Carlo realizations at each stage. The uncertainty estimates for all individual layers were combined into a single matrix and are shown in Figure S1b in the supporting information. The uncertainty of the model beneath the Oregon continental shelf could not be estimated because here we used only one starting model (see section 5.1).

Uncertainty in the crust in the outer portion of the plate (>150 km west of the deformation front) is low with values between 0 and 0.2 km/s generally increasing with depth. Beginning from 150 km west of the deformation front moving landward the uncertainty of a thin zone (100–500 m) located at the top of the crust gradually increases to 0.5–0.7 km/s, while values in the lower crust remain around 0–0.2 km/s (Figure S1). East of the deformation front the zone of high uncertainty in the upper crust expands to a 1.5 km thickness, and uncertainties in the lower crust increase to 0.1–0.4 km/s. In the mantle, uncertainties are generally 0.1 km/s with the exception of the two low-velocity zones that have values up to 0.4 km/s due to the lower ray coverage inherent in low-velocity zones.

6. Analysis and Interpretation of the Velocity Model

In order to interpret our velocity results, we first generated a plausible baseline velocity model based upon a plate cooling model and realistic oceanic lithologies. We then use effective medium theory (with elastic parameters from expected lithologies and alteration products) [*Kuster and Toksöz*, 1974] to infer from our tomography results the amount of porosity, alteration, and water content required to reconcile our results with the baseline model.

6.1. Thermal Modeling

To construct a thermal model for the JdF plate along our model line we first used SEDTEM [*Wang and Davis*, 1992] to calculate the thermal structure west of the deformation front. SEDTEM is a one-dimensional finite element model that accounts for the role of sedimentation on plate cooling. Input parameters appropriate for the JdF plate sediments are taken from *Hyndman and Wang* [1993, Table A1]. Sedimentation rate was estimated from MCS-derived sedimentary thickness. In order to account for the more complicated thermal structure of the accretionary prism and continental margin, we used a 2-D numerical thermal model with kinematic slab and dynamic wedge, following *Syracuse et al.* [2010]. The model incorporates constraints appropriate for our profile: sediment thickness, crustal thickness, crustal age, convergence speed, and the oceanic geotherm derived from SEDTEM at 30 km west of the deformation front. The resulting 2-D temperature model is presented in Figure 5.

6.2. Predicting *Vp* as a Function of Crustal Age and Lithology

We use the temperature dependence of velocity for basalt, gabbro, and peridotite [*Christensen*, 1979] to calculate the predicted age-dependent *Vp* along our profile at three representative depth intervals: the upper crust (0.5–1.5 km below basement, within the dike section), lower crust (2.5–0.5 km above Moho), and upper mantle (0.5–1.5 km below Moho). For each depth interval temperatures were vertically averaged. As reference values for *Vp* for unaltered lithologies at room temperature, we use 6.7 km/s for diabase [*Carlson*, 2014], 7.35 km/s for gabbro [*Miller and Christensen*, 1997], and 8.5 km/s for peridotite [*Ben Ismail and Mainprice*, 1998]. The predicted *Vp* for each lithology as a function of distance along Line 1 is shown in Figure 6, for comparison with the tomography results vertically averaged within each of the depth

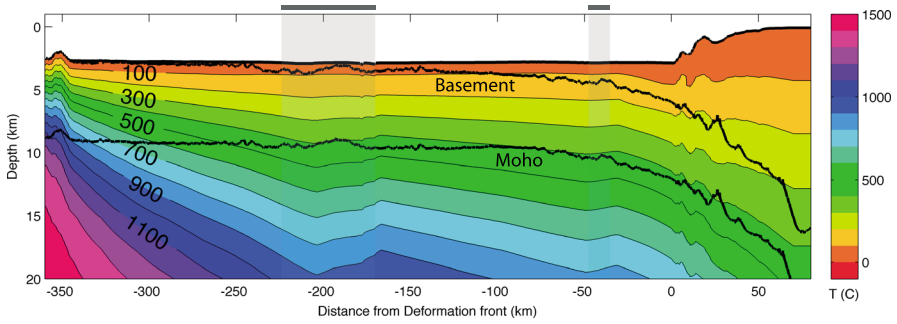

Figure 5. Predicted plate temperature. Gray bars mark locations of propagator wakes. Depth to basement and Moho is shown with bold black lines. The small-scale "bumps" in the isotherms eastward of the deformation front are purely an artifact produced by conforming the thermal structure to the seafloor topography for display purposes.

intervals considered. Differences between the predicted *Vp* and the tomography results are discussed in detail in section 7.

6.3. Water Content Estimates

Porosity in the plate results in reduced seismic wave speeds compared to a nonporous matrix [*Wilkens et al.*, 1991]. We assume that all of the differences in *Vp* between the depth-averaged tomography results and the baseline velocities derived from the thermal model are due to porosity (inherited from accretion at the ridge and/or faulting induced), with cracks and pore space filled with either water or hydrous alteration products. We consider that any potential effects due to changes in anisotropic fabric along the profile or along-profile changes in dominant lithology at each depth interval are negligible. We use effective medium theory as formulated by *Kuster and Toksöz* [1974] to explore the effect on *Vp* of two end-member scenarios: free water

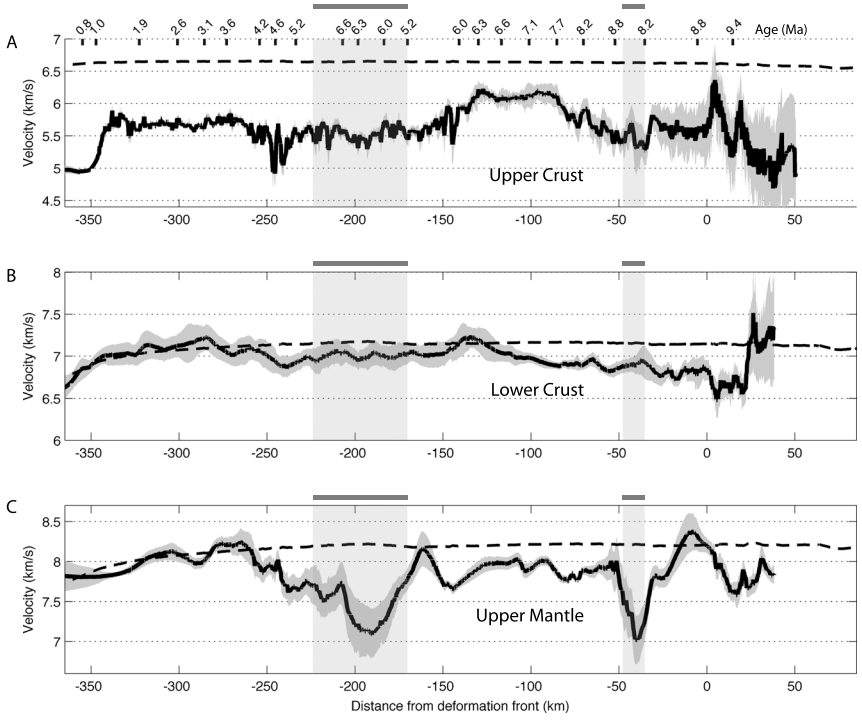

Figure 6. Along line velocity extracted from tomography model (Figure 4) (solid black line) with error bounds (dark gray shaded region) at three depth intervals: (a) upper crust (0.5–1.5 km below basement), (b) lower crust (2.5–0.5 km above Moho), and (c) upper mantle (0.5–1.5 km below Moho) compared to thermal model predicted velocities (dashed lines) for the same depth ranges and an assumed lithology (see text). Gray bars mark locations of propagator wakes. Vertical tick marks in Figure 6a indicate plate age in Ma.

Table 2. Elastic Parameters and Water Content for Water, Alteration Phases, and Protoliths[a]

	K (Gpa)	μ (Gpa)	ρ (g cm^{-3})	Water (wt %)	Vp (km/s)	Vs (km/s)	Aspect Ratio	dVp/dT (km s^{-1} K^{-1})
Brine	2.4[b]	0	1.03 [b]	100	1.50	-	0.01, 0.1	-
MA1	87	47	3.04	1.1	7.00	3.9	0.01	-
MA2	85	44	2.98	0.8	6.94	3.8	0.01	-
Serpentine	43.5	14.5	2.52	12.3[d]	5 [c]	2.4 [c]	0.01	-
Talc	41.5 [e]	22.6 [e]	2.58 [e]	4.7 [d]	5.30	3.0	0.01	-
Diabase	78.3[f]	41[f]	2.93 [f]	-	6.70	3.7	-	−0.00039
Gabbro	96.7 [c]	46.3 [c]	2.94[c]	-	7.35	4.0	-	−0.00057
Peridotite	142.5 [g]	46.3 [g]	3.30	-	8.50	4.6	-	−0.00056

[a] K is bulk modulus, μ is shear modulus, r is density, and T is temperature. MA1, modeled assemblage one contains plagioclase, amphibole, clinopyroxene, and epidote. MA2, modeled assemblage two contains plagioclase, amphibole, and cpx.
[b] *Töksoz et al.* [1976].
[c] *Miller and Christensen* [1997].
[d] *Schmidt and Poli* [1998].
[e] *Bailey and Holloway* [2000].
[f] *Carlson* [2014].
[g] *Ismail and Mainprice* [1998].

and alteration-mineral filled porosity. The effective Vp of a two-phase medium (Vp^*, i.e., our tomographically derived Vp) is a function of the elastic constants of the hydrated porosity medium (infilling alteration products) and that of the dry matrix, the porosity fraction c, and the crack aspect ratio α: $Vp^* = f(K, K', \mu, \mu', \rho, \rho', c, \alpha)$, where K, μ, and ρ are bulk modulus, shear modulus, and density, respectively, and ′ denotes porosity medium. Thus, assuming that the elastic constants of the porosity infilling material, the crack aspect ratio, and its water wt % are known, one can derive porosity fraction c by comparing our tomographically derived P wave velocities with the predicted baseline Vp, and from c the bulk water content of the two-phase medium.

6.3.1. Upper Crust

In the upper crust we only consider the case of porosity in the form of free water filling cracks. We do not consider the case of porosity occupied by alteration minerals because common alteration minerals found in the upper crust such as quartz, epidote, sulfides, zeolites, calcite, and prehnite have elastic constants very similar to those of diabase, thus making Vp insensitive to the amount of alteration in diabase [*Alt et al*., 1986]. Therefore, our water content estimates for the upper crust should be viewed as lower bounds. The aspect ratio of cracks has a strong influence on the effect of porosity on Vp. Aspect ratios of 1 correspond to perfectly spherical inclusions and 0.01 to thin cracks. Using the elastic constant for diabase and brine listed in Table 2 and the formulation of *Kuster and Toksöz* [1974], we find that the observed Vp in the upper crust can be explained by 0.3–0.8 wt % to 0.8–4.0 wt % water, for crack aspect ratios of 0.01 and 0.1, respectively (Figure 7a).

6.3.2. Lower Crust

For the lower crust we consider the case of porosity both in the form of infilling alteration and free water. Where gabbro is exposed to seawater at elevated temperatures there are several possibilities for plausible alteration mineral assemblages. We use the thermodynamic models of *McCollom and Shock* [1998] to define an assemblage of alteration minerals for olivine gabbro at temperatures and pressures appropriate for the lower crust along our profile (Figure 5). At 400°C modeled assemblage MA1 consists of plagioclase (34%), amphibole (45%), clinopyroxene (12%), and epidote (9%) (Table 1), while at 500°C modeled assemblage MA2 is plagioclase (40%), amphibole (43%), and clinopyroxene (17%) (Table 1) [*McCollom and Shock*, 1998]. Elastic parameters for the alteration mineral assemblages at the appropriate pressure and temperatures were calculated using the workbook of *Hacker and Abers* [2004] (Table 2).

Inferred water content in the lower crust derived from our velocity model has a range of 0.0–1.1 wt % water depending on the alteration mineral assemblage considered (Figure 7b). In some instances, modeled velocities in the lower crust are lower than the theoretical velocity of the porosity material. In those cases a maximum value of wt % water equal to the water content of the alteration assemblage is given, as if the protolith had been completely replaced with alteration products. The estimated total amount of water in the plate differs for the two mineral assemblages considered, but the trends of water content are the same for both cases and are discussed in section 7. As an end-member case, we also calculate water contents for

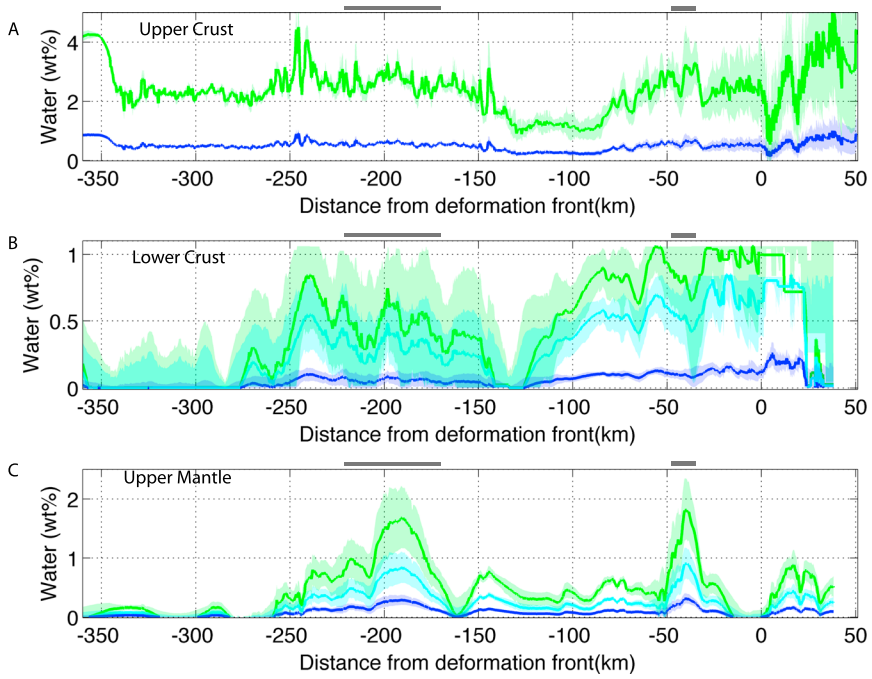

Figure 7. Calculated water content for the three depth intervals. (a) Upper crust (0.5–1.5 km below basement) water content for cracks filled with free water with crack aspect ratios of 0.01, dark blue line, and 0.1, green line, with shaded region corresponding to range of values arising from uncertainty in the velocity model. (b) Lower crust (2.5–0.5 km above Moho) water content for cracks filled with free water (dark blue), mineral assemblage 1 (green), and mineral assemblage 2 (cyan). (c) Upper mantle (0.5–1.5 km below Moho) water content for cracks filled with free water (dark blue), serpentine (green), and talc (cyan). Shaded regions correspond to range of values arising from uncertainty in the velocity model. Gray bars indicate location of propagator wakes.

the lower crust for the case of porosity in the form of free water filling cracks (Figure 7b), which yields a lower bound for the amount of water that can be stored in the lower crust based on our seismic velocity model.

6.3.3. Uppermost Mantle

At pressures above 2 kbar and temperatures over 400°C, serpentine (antigorite) and talc are the expected dominant alteration minerals in a water-saturated average mantle peridotite [e.g., *Schmidt and Poli*, 1998]. For the expected pressures in the uppermost mantle along our transect (<2.5 kbar west of the deformation front) serpentine is stable to ~500°C. At higher temperatures serpentine is converted into forsterite and talc [*Ulmer and Trommsdorff*, 1995]. As estimated temperatures below the Moho along our line are generally 400–500°C reaching a maximum of 550°C at the deformation front (Figure 5), it is likely that the alteration minerals present in the upper mantle are a combination of serpentine and talc and we, therefore, calculate potential water contents for each. Water is predicted to be driven to mantle levels in the outer rise region by subhydrostatic vertical pressure gradients along brittle normal faults [*Faccenda et al*., 2009]; thus, we also calculate free water contents as an end-member case (Figure 7c).

7. Discussion

Our plate-scale seismic velocity model for the Juan de Fuca plate (Figure 4a) bears the imprint of a complex suite of the structure inherited from crustal formation, intraplate stresses, sedimentary loading, off-axis low-temperature hydrothermal alteration, subduction-related bending faulting, and associated alteration. In the following sections, we discuss the velocity variations found at upper crustal, lower crustal, and upper mantle levels, as well as our inferred water content estimates and implications for structure of the plate interior structure away from propagator wakes and away from the region of subduction bending (section 7.1); implications for the influence of propagator wakes on plate structure and hydration (section 7.2); implications for the extent of hydration associated with plate deformation inferred from seismic reflection imaging of crustal and mantle faults (section 7.3); and the mantle hydration of a young, hot subducting oceanic plate (section 7.4).

7.1. Plate Structure Away From Propagator Anomalies and Away From Bending-Related Processes

Our velocities for the upper crust are averaged for a depth interval that encompasses most of seismic layer 2B within the dike section of the oceanic crust and that excludes the uppermost lowest velocity layer of the crust (seismic Layer 2A). Velocities within this upper crustal layer at young ages (<1 Ma) show the largest deviation from the across-plate predicted *Vp* for diabase, ($\Delta Vp \sim -1.7$ km/s), indicating that for such young ages upper crustal velocity is largely controlled by porosity with water contents of up to ~4 wt % (Figures 6 and 7). Between crustal ages of 1.0 and 1.3 Ma (~350 km from the deformation front) velocities increase and free water contents decrease which we attribute to infilling of intrinsic porosity inherited from crustal formation by alteration minerals. For crustal ages of 1.3–6.0 Ma (~350–180 km), the average *Vp* is ~5.6 km/s (Figure 6a), which is similar to the nearly constant 5.4–5.6 km/s velocity found at the top of layer 2B in 0.5–8.3 Ma crust in the superfast spreading southern EPR [*Grevemeyer et al*., 1998]. A previous study across the flanks of the JdFR [*Newman et al*., 2011] found that upper layer 2B reaches a mature *Vp* value of ~5.2 km/s within 0.5 Myr and remains relatively constant afterward out to at least ~3.5 Ma. Our results are consistent with this (note that our upper crustal values represent the average within the dike section, while *Newman et al.* [2011] reported values only for the uppermost part of this layer) and show that within the sedimented JdF plate interior upper crustal structure remains constant beyond 1 Myr in the absence of subduction bending effects (i.e., >150 km from the deformation front) (Figure 6a). The estimated amount of free water stored in this mature, unperturbed upper crust ranges between 0.5 and 2.4 wt % (Figure 7a) depending on the aspect ratio of cracks. The observation that layer 2B velocities remain ~1.1 km/s lower than expected in the dike section to at least until 6 Ma (Figure 6a) and without any apparent correlation with sediment burial (as opposed to the shallower, more porous layer 2A [*Nedimović et al*., 2008]) is consistent with the previous observations of *Newman et al.* [2011]. These authors concluded that layer 2B structure is more dependent on processes occurring at or shortly after accretion than on the evolution of the low-temperature, sediment-controlled shallow hydrothermal system. Exceptions to this are found at basement highs outcropping above the sediments. For example, a local upper crustal velocity low (*Vp* = 5 km/s, 4 wt % water) at ~245 km from the deformation front occurs at a basement high where sedimentary thickness is near zero (Figure 6a). These basement highs may provide permeable pathways for outflow zones for diffuse off-axis hydrothermal circulation [*Fisher et al*., 1990; *Newman et al*., 2011].

The velocity in the lower crust closely matches that predicted by our thermal modeling from 360 to ~140 km west of the deformation front, with the exception of moderately reduced values (−0.2 km/s) across the midplate propagator wake crust (Figure 6b). This indicates that little porosity in the lower crust is inherited at the ridge, and that the lower crust remains dry (or locally hydrated below the levels detectable with our data) outside of the propagator wakes or the region of subduction bending (Figure 7b). This result is in agreement with studies from the southern EPR where no significant age-dependent velocity variations are found in the lower crust between 0.5 and 8.3 Ma, in contrast to velocities at upper crustal and upper mantle depths [*Grevemeyer et al*., 1998]. Within the first ~4.6 Myr (>250 km from the deformation front) velocities in the upper mantle follow predicted velocities (indicating a mostly dry mantle, Figure 7c), after which the influence of propagator wakes (where present) dominates the mantle structure (Figure 6c) and velocities in general are lower than predicted values.

7.2. Influence of Propagator Wakes

Propagator wakes in the interior of the JdF plate are spatially correlated with intraplate seismicity [*Nedimović et al*., 2009]. *Nedimović et al.* [2009] suggest that increased seismicity is due to locally decreased strength inherited from rift propagation caused by the combined weakening effects of more fracturing and fracture-facilitated alteration. Our results support this interpretation: the two propagator wakes transected by our seismic profile are associated with significant velocity and, by inference, hydration anomalies at lower crustal and upper mantle levels, and to a lesser extent in the upper crust (Figures 6 and 7). Near the ridge axis, the wakes of ridge axial discontinuities are known to be associated with prominent negative *P* wave velocity anomalies throughout the crust that reflect greater fracturing within the inner pseudofault than in the surrounding crust [e.g., *Canales et al*., 2003; *Weekly et al*., 2014]. We find that upper crustal (layer 2B) velocities within the propagator wakes are only slightly reduced relative to neighboring crust, suggesting more modest fracturing and/or alteration (Figure 6a). This observation is consistent with the findings of *Newman et al.* [2011] of moderate upper layer 2B velocity decreases within propagator wakes that coincide with increased

lower layer 2A velocities interpreted as the result of enhanced fluid flow and mineral precipitation [*Nedimović et al.*, 2008]. Our results predict upper crust within propagator wakes that is only moderately more hydrated than unperturbed crust of similar age (Figure 7a).

In the lower crust, however, broad regions of small velocity anomalies of −0.1 km/s are found in our model (Figure 6b). The anomalies in the lower crust are less localized to the propagator wake zones, compared with the anomalies in the uppermost mantle, extending some 20 km beyond the boundaries of the propagator wake. An anomaly of −0.1 km/s corresponds to estimated chemically bounded water contents of 0.25–0.8 wt % (depending on the alteration mineral assemblage assumed, Table 2) or alternatively to less than 0.1 wt % if we assume all water is stored as a free phase in the pore spaces (Figure 7b).

At mantle levels the propagator wakes are associated with the lowest mantle velocities found anywhere along our plate transect ($\Delta Vp < -1$ km/s, Figure 6c). This is consistent with findings of low *Vp* (7–7.2 km/s) across other propagator wakes in the northern part of the JdF plate [*McClymont and Clowes*, 2005] and indicates significant local alteration and hydration of the mantle. While the lateral extents of the two propagator wakes transected by our profile are significantly different (50 km versus 10 km) the magnitudes of the velocity anomalies are similar. Interestingly, seismic reflection imaging [*Han et al.*, 2016] indicates that Moho reflections are weak to absent within the zone of the larger propagator wake. This difficulty in imaging Moho indicates a very low velocity gradient across the crust/mantle transition that is consistent with the local low *Vp* values found in the mantle (Figure 6c).

The very weak (or absence of) Moho reflections in the MCS data are also consistent with our OBS data that show markedly different *Pg-PmP-Pn* triplications for waves sampling the propagator wakes compared with those from waves sampling normal crust. For example, record sections from instruments 70 and 71 (Figures S30 and S31) located near the western edge of the propagator wake (Figure 4a) display very well defined triplications with high-amplitude *PmP* (which suggests sharp velocity contrast at the Moho) for shots to the west of the OBSs that sample normal crust (~20–60 km negative ranges). In contrast to this, shots to the east of the OBSs that sample propagator crust (~20–60 km positive ranges) display weak *PmP* and less defined triplications, suggesting a more gradual velocity increase through the Moho. The same pattern is observed on instruments 67 and 68 (Figures S27 and S28) located near the eastern edge of the propagator (Figure 4a): well-defined triplications for shots to the east of the instrument (positive ranges), but weaker *PmP* and less defined triplication for shots to the west of the instruments (negative ranges). Data from instrument 69 (Figure S29), which is located near the center of the propagator wake (Figure 4a), have low-amplitude *PmP* arrivals and lack clear triplication for shots both to the east and west of the OBS. All of these observations are consistent with the subdued velocity contrast at the crust/mantle transition in the propagator wake zones in our final velocity model (Figure 4a).

If we assume serpentinization is the alteration process, the JdF plate mantle could be locally hydrated with up to 1.8 wt % water beneath propagator wakes (Figure 7c), which corresponds to a 15% maximum value of serpentinization. However, our thermal model predicts sub-Moho temperatures that are too high (>400°C) for significant serpentine formation, but within the stability field of other hydrated minerals such as talc. If talc is the dominant hydration mineral, then water contents could be lower (0.9 wt %, Figure 7c). Alternatively, the extensive fracturing and shearing of the crust at propagating ridge offsets [*Hey et al.*, 1980; *Wilson et al.*, 1988] may enhance convective cooling, resulting in locally cooler mantle within the propagator wakes than predicted by our plate thermal model, thus facilitating mantle serpentinization. In addition to chemically bounded water, open fractures at sub-Moho levels may contain free water. Under this assumption, propagator wakes may contain up to 0.1–0.3 wt % water in open fractures (Figure 7c). However, the same assumption yields a lower amount of free water in the lower crust (<0.1 wt %, Figure 7b), and it is difficult to explain how more water could be retained in open fractures at mantle levels than at lower crustal levels. Thus, we conclude that the large negative velocity anomalies present at both propagator wakes in the uppermost mantle are, at least in part, due to serpentinization of the mantle and/or presence of other hydrated minerals such as talc.

7.3. Deformation Effects in Plate Seismic Structure

Previous studies have revealed faults within the sediment section blanketing the JdF plate at distances of up to 200 km west of the deformation front (Figure 4c) and one region of crustal-scale faulting [*Nedimović et al.*, 2009]. Reflection images derived from the collocated MCS data acquired along our Oregon transect

presented in *Han et al.* [2016] reveal faults within the sediments and faint fault reflections in the upper crust at distances up to 320 km seaward of the deformation front. Sediment and crustal faults are sparse and heterogeneous in distribution west of 130–140 km from the deformation front, but increase in density at closer distances, with numerous faults within the sediments and crust at distances <130 km, as well as a prominent group of ridgeward dipping lower crustal reflectors (LCRs) found 70–150 km from the deformation front (Figure 4c). Plate bending due to the combined effects of sediment loading and subduction begins at 145–150 km west of the deformation front, as inferred from residual basement topography after correcting for plate cooling [*Han et al*., 2016]. Removing the predicted effects of sediment loading from the basement topography, bending due to subduction is inferred to initiate ~75–80 km from the deformation front. Within 40 km from the deformation front, sediment fault throws increase, and reflective faults that transect the entire crust and extend 6–7 km into the upper mantle are observed (Figure 4c). From these observations *Han et al.* [2016] conclude that most deformation associated with plate bending occurs at distances <40 km from the deformation front.

Our plate-scale velocity model reveals significant changes in structure within this same distance range. Some of this variability can be associated with the onset of plate deformation due to subduction bending and sediment loading, while other structures may have been inherited from ridge accretionary processes.

7.3.1. Upper Crust

At ~150 km from the deformation front, upper crustal velocities increase rapidly from 5.6 km/s found in 1.3–6.0 Ma crust to quite uniform values of ~6.1 km/s in 6.3–7.8 Ma crust (Figure 6a). This change in upper crustal structure is spatially coincident with changes in crustal reflectivity and sediment fault distribution [*Han et al*., 2016] including (1) the presence of LCRs in 6–8 Ma crust, and (2) a transition from sparsely distributed sediment faults to high sediment fault density at 140 km from the deformation front (Figure 4c). LCRs are mid-to-lower crustal low-angle reflections interpreted as shear zones formed at the ridge crest during periods of buoyant mantle flow that is faster than plate motion [*Bécel et al*., 2015; *Han et al*., 2016; *Kodaira et al*., 2014]. The spatial correlation of the zone of high upper crustal *Vp* with the LCRs suggests that the anomalous upper crustal structure could also be inherited from such period of anomalous crustal formation. Although the origin of LCRs is unclear, it is possible that an upper crust with lower porosity and hence higher *Vp* was formed along with them. An argument against this hypothesis is that in the only other region where these features have been observed and seismic velocity information is available, there is no evidence for similar increased upper crustal velocities [*Kodaira et al*., 2014].

Alternatively, the coincident increase in both the upper crustal *Vp* at 6.0–6.3 Ma crust (Figure 6a) and the sediment fault density suggests that processes related to or controlled by the deformation of the plate may play a role. The earlier study of *Nedimović et al.* [2008] from the JdF plate interior indicates that hydrothermal circulation and precipitation of alteration minerals infilling porosity inherited from accretion at the ridge axis in the uppermost crust are ongoing to the end of their study area at 150 km from the spreading ridge. At this distance from the ridge axis, Layer 2A velocities are still significantly below 4.0 km/s [*Nedimović et al*., 2008] and hence less than the expected mature Layer 2A velocity of ~4.3 km/s [*Grevemeyer et al*., 1999] within the discussed area of increased fault density. With the higher sediment fault density beginning in ~6 Ma crust, perhaps faulting and fracturing reach deeper into the dike section leading to deeper penetrating ridge flank hydrothermal circulation and clogging of intrinsic porosity with mineral precipitation. Closer to the deformation front upper crustal velocities decrease to values comparable to and in places, slightly lower than found in younger pre-6 Ma crust. Here the landward reduction in *Vp* may be a consequence of the documented increased faulting in this region due to plate bending, with the effects of faulting in velocity canceling and outpacing any velocity increase due to mineral precipitation processes.

Approaching the deformation front *Vp* uncertainty increases significantly (Figure 6a); however, immediately to the east of the deformation front two narrow upper crustal anomalies ($Vp > 6$ km/s) with low water content (Figure 7a) could indicate localized zones of dehydration of the downgoing plate, perhaps contributing to the abundant fluid production in the accretionary prism at Hydrate Ridge [*Trehu et al*., 2004].

7.3.2. Lower Crust

From near the ridge axis to 135–145 km from the deformation front and just east of the wide propagator wake, lower crustal velocities have values indicating dry gabbros (Figure 6b). Starting from 130 km west of the deformation front, *P* wave velocities in the lower crust show a long-wavelength decreasing trend (Figure 6b), which is coincident with the initiation of plate deformation due to sediment loading and

subduction bending around 145 km and with the development of faint possible trenchward dipping faulting in the lower crust (Figure 4c) [*Han et al*., 2016]. Although the onset of this decreasing lower crustal *Vp* is also spatially coincident with the appearance of LCRs, the large-scale decreasing trend in *Vp* is continuous to the deformation front, well east of the LCR crust (Figure 6b). We attribute the progressive decrease in velocities in the lower crust to increased porosity caused by sediment loading and bending-related strain that initially produces fractures and fault zones that are too small or close to the limit of what can be resolved with the MCS data. Hydration of the lower crust after the onset of bending-related faulting can be up to 1 wt % in chemically bounded water or as little 0.2 wt % if all water is stored as a free fluid phase in pore spaces (Figure 7b).

7.3.3. Upper Mantle

Between 150 and 50 km west of the deformation front, mantle velocities are relatively low (0.25–0.50 km/s) with respect to predicted values, suggesting greater fracturing and hydration in this region (Figure 6c). Along this section of the profile, a cluster of landward dipping events is imaged from ~110 to 130 km attributed to mantle shears associated with LCR formation, but no reflections interpreted as through-crust faults penetrating into the mantle are imaged in the reflection data (Figure 4c) [*Han et al*., 2016]. The reduced mantle velocities could be due to local anisotropy anomalies induced by mantle shears, or alternatively, due to faulting at scales smaller than can be detected given the resolution of the reflection imaging. If the latter, then some mantle hydration at this location can be inferred from the seismic velocities. Modeled temperatures at the Moho along this section are ~450°C (Figure 5), indicating that talc rather than serpentine is probably the primary mode of hydration in this part of the system. In the case of talc alteration, the moderate decrease in mantle velocity is consistent with only $<$0.2 wt % water at upper mantle levels as a consequence of plate bending processes.

Closer to the deformation front (at distances between 34 and 13 km) deeply penetrating faults extending 6–7 km into the upper mantle are clearly imaged immediately east of the small propagator wake (Figure 4c) [*Han et al*., 2016]. As discussed above, a prominent mantle velocity anomaly is associated with the propagator wake, with a low centered at 40 km and rapid eastward increase, reaching (or exceeding) normal "dry" mantle velocities locally ~10 km seaward of the trench (Figure 6c). The zone of deep-penetrating faults falls within the region of increasing mantle velocities immediately to the east of the small propagator. Mantle water contents of $<$1 wt % (Figure 7c) are estimated for this region, consistent with values reported by *Han et al.* [2016] based on estimates of the volume of the imaged fault zones. There is no clear explanation for why, within 15 km of the deformation front, our mantle velocities reach predicted dry values (Figure 6c). Mantle reflectivity is also absent within 14 km of the deformation front consistent with less deep fracturing and alteration [*Han et al*., 2016]. In addition, seismic data from a fan profile recorded at this location during our experiment shows a complex mantle anisotropic signature that cannot be explained by simple olivine alignment along the spreading direction [*Canales et al*., 2014]. It is possible that the elevated mantle velocities we find immediately west of the deformation front may be partly associated with an anomalous mantle anisotropic structure in the paleosegment east of the 8.2–8.8 Ma propagator. Regardless of this, the mantle velocities approaching and across the deformation front suggest that the oceanic mantle of the paleosegment currently being and about to be subducted beneath the Cascadia deformation front at this latitude is only very mildly hydrated (Figure 7c).

7.4. Mantle Hydration of a Young, Hot Subducting Oceanic Plate

Active source experiments at other subduction zones have found values of upper mantle hydration in the incoming plate at the onset of subduction of up to 3.5 wt % water off central and NW Nicaragua [*van Avendonk et al*., 2011], 1–2 wt % water off SE Nicaragua [*Ivandic et al*., 2008; *van Avendonk et al*., 2011], and 0–3 wt % water off south-central Chile [*Contreras-Reyes et al*., 2007]. Along our transect of the JdF plate, the inferred extent of mantle hydration is somewhat lower and locally variable with values between 0 and 1.8 wt % (Figure 7c) and we expect water delivery to the deep portions of the Cascadia subduction zone to be highly variable both spatially and through time. Directly west of the deformation front a local mantle velocity high is found (Figure 6c) consistent with predicted values for dry upper mantle. However, pronounced velocity anomaly lows indicating locally enhanced hydration of the uppermost mantle are associated with the propagator wakes located farther west (Figure 6c). As they subduct, these hydration anomalies will result in local zones of increased water delivery. *Nedimović et al.* [2009] relate the increased seismicity beneath the Olympic peninsula in part to the presence of a subducted propagator wake. In Cascadia the pressure-temperature conditions in the uppermost mantle are at the edge of the stability zone

for serpentine but are suitable for the formation of other hydrated alteration minerals such as talc. However, even if talc is the primary style of mantle hydration of the incoming plate beneath Cascadia, the amount of water stored at mantle levels in the downgoing JdF plate is very limited, with most of the water likely carried down at crustal levels.

8. Conclusions

We have used wide-angle seismic data to obtain a 2-D *P* wave tomography model of the Juan de Fuca plate along a profile extending from the flank of Axial seamount to offshore central Oregon. Our results show variations in crustal and upper mantle structure that we interpret as resulting from variations in porosity and extent of hydration of the oceanic plate prior to subduction beneath the Cascadia forearc. We conclude the following.

1. Within the plate interior, away from the influence of plate bending processes, the JdF crust (below seismic layer 2A) and mantle acquire a mature structure within 1 Myr after accretion. This mature structure is characterized by an upper crust with average velocity of 5.6 km/s within the dike section (layer 2B), from which we infer a water content of 0.5–2.1 wt % (depending on the dominant shape of water-filled pores assumed), and a lower crust and uppermost mantle with seismic velocities consistent with dry gabbro and peridotite, respectively, at the temperatures expected from a cooling plate model.
2. Our profile crosses the wakes of two propagators formed at the paleo JdFR, which are associated with velocity and hydration anomalies at lower crustal and upper mantle levels, and to a lesser extent in the upper crust. Within the lower crust, we estimate water contents of 0.25–0.8 wt % if we assume that water is chemically bound in alteration mineral assemblages or as little as $<$0.1 wt % if water is stored as a fluid phase in pore spaces. We find large low-velocity anomalies in the mantle (at 0.5–1.5 km below basement) at the location of the propagators, which we interpret as resulting from local mantle hydration (up to 0.9–1.8 wt % if mantle hydration occurs in the form of talc or serpentine, respectively, or as little as 0.2 wt % of free water). Thus, paleosegment boundaries (i.e., propagator wakes) are zones of enhanced hydration that may at least locally affect subduction zone processes.
3. At a distance of ~150 km from the Cascadia deformation front, we find changes in upper crustal velocity structure that correlate spatially with both the onset of plate deformation due to the combined effects of subduction bending and sediment loading, as well as with the location of lower crustal reflectivity interpreted as inherited from a period of anomalous ridge accretionary processes [*Han et al*., 2016]. The observed increase in upper crustal velocity could be an intrinsic feature related to the formation of this lower crustal reflectivity, or alternatively, could be related to changes in the midplate hydrothermal system triggered by onset of plate bending-related deformation.
4. The onset of bending-related faulting results in progressive decrease in lower crustal seismic velocities toward the deformation front. We estimate that this velocity decrease can be explained by hydration of the lower crust, with up to 1 wt % if water is chemically bounded in alteration mineral assemblages or as little as 0.2 wt % of free water.
5. Within 150–50 km west of the deformation front, away from a small propagator wake zone, mantle velocities are slightly lower than predicted for dry upper mantle compositions, consistent with limited alteration of the mantle. In the vicinity of the deformation front at distances 15–30 km where deep-penetrating faults are imaged in MCS data, less than 1 wt % mantle hydration in the uppermost 1–2 km is found. In the region of the deformation front mantle hydration is both spatially heterogeneous and very limited with values between 0 and 0.3 wt % water.
6. All our observations lead us to conclude that the paleosegment currently being subducted beneath the Cascadia deformation front offshore central Oregon is very mildly hydrated, if not dry, at mantle levels, with most of the water that is supplied into the subduction system being stored at crustal levels.

Acknowledgments

9We are grateful to Captain Mark Landow (R/V *Marcus Langseth* cruise MGL1211) and Captain Jeff Crews (R/V *Oceanus* cruise OC1206A), and the crews, technical staff, and scientific party during both cruises for their valuable assistance in collecting the data. We thank the OBSIP Management Office and the personnel of the SIO and WHOI Institutional Instrument Contributors for their technical support and excellent skills during OBS operations. We would also like to thank Kelin Wang for providing the SEDTEM code and the Associate Editor and two anonymous reviewers who provided excellent feedback. This research was supported by NSF grants OCE-1029305 to J.P.C., OCE-1029411 to S.M.C., H.C, and M.R.N., and OCE-1249353 to P.v.K. Data used in this research were provided by instruments from the Ocean Bottom Seismograph Instrument Pool (http://www.obsip.org) which is funded by the National Science Foundation. OBSIP data are archived at the IRIS Data Management Center (http://www.iris.edu) under code X6 (doi:10.7914/SN/X6_2012).

References

Alt, J. C., J. Honnorez, C. Laverne, and R. Emmerman (1986), Hydrothermal alteration of a 1 km section through the upper oceanic crust, Deep Sea Drilling Project Hole 504B: Mineralogy, chemistry, and evolution of sea-water-basalt interactions, *J. Geophys. Res.*, *91*, 10,309–10,335, doi:10.1029/JB091iB10p10309.

Arnulf, A. F., A. J. Harding, G. M. Kent, S. M. Carbotte, J. P. Canales, and M. R. Nedimović (2014), Anatomy of an active submarine volcano, *Geology*, *42*(8), 655–658.

Audet, P., M. G. Bostock, N. I. Christensen, and S. M. Peacock (2009), Seismic evidence for overpressured subducted oceanic crust and megathrust fault sealing, *Nature*, *457*, 76–78.

Bailey, E., and J. R. Holloway (2000), Experimental determination of elastic properties of talc to 800°C, 0.5 GPa; calculations of the effect on hydrated peridotites, and implications for cold subduction zones, *Earth Planet. Sci. Lett.*, *183*, 487–498.

Bécel, A., D. J. Shillington, M. R. Nedimović, S. C. Webb, and H. Kuehn (2015), Origin of dipping structures in fast-spreading oceanic lower crust offshore Alaska imaged by multichannel seismic data, *Earth Planet. Sci. Lett.*, *424*, 26–37.

Ben Ismail, W., and D. Mainprice (1998), An olivine fabric database: An overview of upper mantle fabrics and seismic anisotropy, *Tectonophysics*, *296*(1-2), 145–157.

Billen, M. I., and M. Gurnis (2001), A low viscosity wedge in subduction zones, *Earth Planet. Sci. Lett.*, *193*(1-2), 227–236.

Bostock, M. G., R. D. Hyndman, S. Rondenay, and S. M. Peacock (2002), An inverted continental Moho and serpentinization of the forearc mantle, *Nature*, *417*, 536–538.

Canales, J. P., and S. M. Carbotte (2012), Evolution and hydration of the Juan de Fuca crust and uppermost mantle, International Federation of Digital Seismograph Networks. Other/Seismic Network, doi:10.7914/SN/X6_2012.

Canales, J. P., R. S. Detrick, D. R. Toomey, and W. S. D. Wilcock (2003), Segment-scale variations in the crustal structure of 150–300 kyr old fast spreading oceanic crust (East Pacific Rise, 8°15′N-10°15′N) from wide-angle seismic refraction profiles, *Geophys J. Int.*, *152*, 766–794.

Canales, J. P., R. S. Detrick, S. M. Carbotte, G. M. Kent, J. B. Diebold, A. J. Harding, J. Babcock, M. R. Nedimović, and E. van Ark (2005), Upper crustal structure and axial topography at intermediate-spreading ridges: Seismic constraints from the Southern Juan de Fuca ridge, *J. Geophys. Res.*, *110*, B12104, doi:10.1029/12005JB003630.

Canales, J. P., S. M. Carbotte, H. D. Carton, and M. R. Nedimović (2014), State of Hydration of the Juan de Fuca Plate Along the Cascadia Deformation Front from Controlled-Source Wide-Angle Seismic Data, Abstract T51B-4615 presented at 2014 Fall Meeting, *AGU, San Francisco, Calif.*, 15–19 Dec.

Carbotte, S. M., R. S. Detrick, A. J. Harding, J. P. Canales, J. Babcock, G. M. Kent, E. van Ark, M. R. Nedimović, and J. B. Diebold (2006), Rift topography linked to magmatism at the intermediate spreading Juan de Fuca ridge, *Geology*, *34*(3), 209–212.

Carbotte, S. M., M. R. Nedimović, J. P. Canales, G. M. Kent, A. J. Harding, and M. Marjanović (2008), Variable crustal structure along the Juan de Fuca ridge: Influence of on-axis hotspots and absolute plate motions, *Geochem. Geophys. Geosyst.*, *9*, Q08001, doi:10.1029/02007GC001922.

Carbotte, S. M., J. P. Canales, H. Carton, and M. R. Nedimović (2014), Multi-channel seismic shot data from the Cascadia subduction zone acquired during the R/V *Marcus Langseth* expedition MGL1211 (2012), Integrated Earth Data Applications (IEDA).

Carlson, R. L. (2014), The influence of porosity and crack morphology on seismic velocity and permeability in the upper oceanic crust, *Geochem. Geophys. Geosyst.*, *15*, 10–27, doi:10.1002/2013GC004965.

Christensen, N. I. (1979), Compressional wave velocities in rocks at high temperatures and pressures, critical thermal gradients, and crustal low-velocity zones, *J. Geophys. Res.*, *84*, 6849–6857, doi:10.1029/JB084iB12p06849.

Contreras-Reyes, E., I. Grevemeyer, E. R. Flueh, M. Scherwath, and M. Heesemann (2007), Alteration of the subducting oceanic lithosphere at the southern central Chile trench-outer rise, *Geochem. Geophys. Geosyst.*, *8*, Q07003, doi:10.1029/02007GC001632.

Davis, E. E., K. Wang, J. He, D. S. Chapman, H. Villinger, and A. Rosenberger (1997), An unequivocal case for high Nusselt number hydrothermal convection in sediment-buried igneous oceanic crust, *Earth Planet. Sci. Lett.*, *146*, 137–150.

Dragert, H., K. L. Wang, and T. S. James (2001), A silent slip event on the deeper Cascadia subduction interface, *Science*, *292*(5521), 1525–1528.

Elderfield, H., and A. Schulz (1996), Mid-ocean ridge hydrothermal fluxes and the chemical composition of the ocean, *Ann. Rev. Earth Planet. Sci.*, *24*, 191–224.

Escartín, J., G. Hirth, and B. Evans (2001), Strength of slightly serpentinized peridotites: Implications for the tectonics of oceanic lithosphere, *Geology*, *29*(11), 1023–1026.

Faccenda, M., T. V. Gerya, and L. Burlini (2009), Deep slab hydration induced by bending-related variations in tectonic pressure, *Nat. Geosci.*, *2*, 790–793, doi:10.1038/NGEO1656.

Fisher, A. T., K. Becker, T. N. Narasimhan, M. G. Langseth, and M. J. Mottl (1990), Passive, off-axis convection through the southern flank of the Costa Rica Rift, *J. Geophys. Res.*, *95*, 9343–9370, doi:10.1029/JB095iB06p09343.

Gerdom, M., A. M. Trehu, E. R. Flueh, and D. Klaeschen (2000), The continental margin off Oregon from seismic investigations, *Tectonophysics*, *329*, 79–97.

Grevemeyer, I., W. Weigel, and C. Jennrich (1998), Structure and ageing of oceanic crust at 14°S on the East Pacific Rise, *Geophys J. Int.*, *135*, 573–584.

Grevemeyer, I., N. Kaul, H. Villinger, and W. Weigel (1999), Hydrothermal activity and the evolution of the seismic properties of upper oceanic crust, *J. Geophys. Res.*, *104*, 5069–5079, doi:10.1029/1998JB900096.

Hacker, B. R. (2008), H_2O subduction beyond arcs, *Geochem. Geophys. Geosyst.*, *9*, Q03001, doi:10.1029/2007GC001707.

Hacker, B. R., and G. A. Abers (2004), Subduction Factory 3: An excel worksheet and macro for calculating the densities, seismic wave speeds, and H_2O contents of minerals and rocks at pressure and temperature, *Geochem. Geophys. Geosyst*, *5*(1).

Hacker, B., S. M. Peacock, G. A. Abers, and S. D. Holloway (2003), Subduction factory: 2. Are intermediate-depth earthquakes in subducting slabs linked to metamorphic dehydration reactions?, *J. Geophys. Res.*, *108*(B1), 2030, doi:10.1029/2001JB001129.

Han, S., S. M. Carbotte, J. P. Canales, M. R. Nedimović, H. Carton, J. C. Gibson, and G. W. Horning (2016), Seismic reflection imaging of the Juan de Fuca plate from ridge to trench: New constraints on the distribution of faulting and evolution of the crust prior to subduction, *J. Geophys. Res. Solid Earth*, *121*, 1849–1872, doi:10.1002/2015JB012416.

Hey, R. N., F. K. Dunnebier, and W. J. Morgan (1980), Propagating rifts on mid-ocean ridges, *J. Geophys. Res.*, *85*, 3647–3658, doi:10.1029/JB085iB07p03647.

Hirth, G., J. Escartín, and J. Lin (1998), The rheology of the lower oceanic crust: Implications for lithospheric deformation at mid-ocean ridges, in *Faulting and Magmatism at Mid-Ocean Ridges*, edited by W. R. Buck et al., pp. 291–303, AGU, Washington, D. C.

Hunter, A. G., P. D. Kempton, and P. Greenwood (1999), Low-temperature interaction—An isotopic and mineralogical perspective of upper crustal evolution, eastern flank of the Juan de Fuca ridge (JdFR), ODP Leg 168, *Chem. Geol.*, *155*(1-2), 3–28.

Hyndman, R. D., and K. Wang (1993), Thermal constraints on the zone of major thrust earthquake failure: The Cascadia subduction zone, *J. Geophys. Res.*, *98*, 2039–2060, doi:10.1029/92JB02279.

Ismail, W. B., and D. Mainprice (1998), An olivine fabric database: An overview of upper mantle fabrics and seismic anisotropy, *Tectonophysics*, *296*(1-2), 145–157.

Ivandic, M., I. Grevemeyer, A. Berhorst, E. R. Flueh, and K. McIntosh (2008), Impact of bending related faulting on the seismic properties of the incoming oceanic plate offshore of Nicaragua, *J. Geophys. Res.*, *113*, B05410, doi:10.1029/02007JB005291.

Kao, H., S. J. Shan, H. Dragert, G. Rogers, J. F. Cassidy, and K. Ramachandran (2005), A wide depth distribution of seismic tremors along the northern Cascadia margin, *Nature*, *436*(7052), 841–844.

Kao, H., K. Wang, R. Y. Chen, I. Wada, J. H. He, and S. D. Malone (2008), Identifying the rupture plane of the 2001 Nisqually, Washington, earthquake, *Bull. Seismol. Soc. Am.*, *98*(3), 1546–1558.
Karsten, J. L., and J. R. Delaney (1989), Hot spot-ridge crest convergence in the northeast Pacific, *J Geophys Res.*, *94*, 700–712, doi:10.1029/JB094iB01p00700.
Kawakatsu, H., and S. Watada (2007), Seismic evidence for deep-water transportation in the mantle, *Science*, *316*, 1468–1471.
Kodaira, S., G. Fujie, M. Yamashita, T. Sato, T. Takahashi, and N. Takahashi (2014), Seismological evidence of mantle flow driving plate motions at a palaeo-spreading centre, *Nat. Geosci.*, *7*(5), 371–375.
Korenaga, J., W. S. Holbrook, G. M. Kent, P. B. Kelemen, R. S. Detrick, H.-C. Larsen, J. R. Hopper, and T. Dahl-Jensen (2000), Crustal structure of the southeast Greenland margin from joint refraction and reflection seismic tomography, *J. Geophys. Res.*, *105*, 21,591–21,614, doi:10.1029/2000JB900188.
Kuster, G. T., and M. N. Toksöz (1974), Velocity and attenuation of seismic waves in two-phase media: Part I. Theoretical formulations, *Geophysics*, *39*(5), 587–606.
Lécuyer, C., and B. Reynard (1996), High-temperature alteration of oceanic gabbros by seawater (Hess Deep, Ocean Drilling Program Leg 147): Evidence from oxygen isotopes and elemental fluxes, *J. Geophys. Res.*, *101*, 15,883–15,897, doi:10.1029/96JB00950.
Marjanović, M., S. M. Carbotte, M. R. Nedimović, and J. P. Canales (2011), Gravity and seismic study of crustal structure along the Juan de Fuca ridge axis and across pseudofaults on the ridge flanks, *Geochem. Geophys. Geosyst.*, *12*, Q05008, doi:10.1029/2010GC003439.
McClymont, A. F., and R. M. Clowes (2005), Anomalous lithospheric structure of northern Juan de Fuca plate—A consequence of oceanic rift propagation? *Tectonophysics*, *406*, 213–231.
McCollom, T. M., and E. L. Shock (1998), Fluid-rock interactions in the lower oceanic crust: Thermodynamic models of hydrothermal alteration, *J. Geophys. Res.*, *103*, 547–575, doi:10.1029/97JB02603.
McCrory, P. A., and D. S. Wilson (2013), A kinematic model for the formation of the Siletz-Crescent forearc terrane by capture of coherent fragments of the Farallon and Resurrection plates, *Tectonics*, *32*, 718–736, doi:10.1002/tect.20045.
Miller, D. J., and N. I. Christensen (1997), Seismic velocities of lower crustal and upper mantle rocks from the slow spreading Mid-Atlantic Ridge, south of the Kane transform zone (MARK), *Proc. ODP, Sci. Results*, *153*, 437–454.
Nedimović, M. R., R. D. Hyndman, K. Ramachandran, and G. D. Spence (2003), Reflection signature of seismic and aseismic slip on the northern Cascadia subduction interface, *Nature*, *424*, 416–420.
Nedimović, M. R., S. M. Carbotte, A. J. Harding, R. S. Detrick, J. P. Canales, J. B. Diebold, G. M. Kent, M. Tischer, and J. Babcock (2005), Frozen magma lenses below the oceanic crust, *Nature*, *436*, 1149–1152.
Nedimović, M. R., S. M. Carbotte, J. B. Diebold, A. J. Harding, J. P. Canales, and G. M. Kent (2008), Upper crustal evolution across the Juan de Fuca ridge flanks, *Geochem. Geophys. Geosyst.*, *9*, Q09006, doi:10.1029/02008GC002085.
Nedimović, M. R., D. R. Bohnenstiehl, S. M. Carbotte, J. P. Canales, and R. P. Dziak (2009), Faulting and hydration of the Juan de Fuca plate system, *Earth Planet. Sci. Lett.*, *284*, 94–102.
Newman, K. R., M. R. Nedimović, J. P. Canales, and S. M. Carbotte (2011), Evolution of seismic layer 2B across the Juan de Fuca ridge from hydrophone streamer 2D traveltime tomography, *Geochem. Geophys. Geosyst.*, *12*, Q05009, doi:10.1029/2010GC003462.
Obara, K. (2002), Nonvolcanic deep tremor associated with subduction in southwest Japan, *Science*, *296*(5573), 1679–1681.
Peacock, S. M. (2001), Are the lower zones of double seismic zones caused by serpentine dehydration in subduction oceanic mantle?, *Geology*, *29*(4), 299–302.
Preston, L. A., K. C. Creager, R. S. Crosson, T. M. Brocher, and A. M. Trehu (2003), Intraslab earthquakes: Dehydration of the Cascadia slab, *Science*, *302*, 1197–1200.
Ranero, C. R., J. Phipps Morgan, K. McIntosh, and C. Reichert (2003), Bending-related faulting and mantle serpentinization at the Middle America trench, *Nature*, *425*, 367–373.
Rogers, G., and H. Dragert (2003), Episodic tremor and slip on the Cascadia subduction zone: The chatter of silent slip, *Science*, *300*, 1942–1943.
Rüpke, L. H., J. Phipps Morgan, M. Hort, and J. A. D. Connolly (2004), Serpentine and the subduction zone water cycle, *Earth Planet. Sci. Lett.*, *223*, 17–34.
Schmidt, M. W., and S. Poli (1998), Experimentally based water budgets for dehydrating slabs and consequences for arc magma generation, *Earth Planet. Sci. Lett.*, *163*, 361–379.
Syracuse, E. M., P. E. van Keken, and G. A. Abers (2010), The global range of subduction zone thermal models, *Phys. Earth Planet. In.*, *183*(1-2), 73–90.
Tatsumi, Y. (1989), Migration of fluid phases and genesis of basalt magmas in subduction zones, *J. Geophys. Res.*, *94*, 4697–4707, doi:10.1029/JB094iB04p04697.
Töksoz, M. N., Q. C. Cheng, and A. Timur (1976), Velocities of seismic waves in porous rocks, *Geophysics*, 41, 621–645, doi:10.1190/1.1440639.
Tréhu, A. M., I. Asudeh, T. M. Brocher, J. H. Luetgert, W. D. Mooney, J. L. Nabelek, and Y. Nakamura (1994), Crustal architecture of the Cascadia forearc, *Science*, *266*, 237–243.
Trehu, A. M., et al. (2004), Three-dimensional distribution of gas hydrate beneath southern Hydrate Ridge: Constraints from ODP Leg 204, *Earth Planet. Sci. Lett.*, *222*, 845–862.
Ulmer, P., and V. Trommsdorff (1995), Serpentine stability to mantle depths and subduction-related magmatism, *Science*, *268*, 858–861.
van Avendonk, H. J. A., A. J. Harding, J. A. Orcutt, and J. S. McClain (1998), A two-dimensional tomography study of the Clipperton transform fault, *J. Geophys. Res.*, *103*, 17,885–17,899, doi:10.1029/98JB00904.
van Avendonk, H. J. A., W. S. Holbrook, D. Lizarralde, and P. Denyer (2011), Structure and serpentinization of the subducting Cocos plate offshore Nicaragua and Costa Rica, *Geochem. Geophys. Geosyst.*, *12*, Q06009, doi:10.1029/2011GC003592.
van Keken, P. E., B. R. Hacker, E. M. Syracuse, and G. A. Abers (2011), Subduction factory: 4. Depth-dependent flux of H_2O from subducting slabs worldwide, *J. Geophys. Res.*, *116*, B01401, doi:10.1029/02010JB007922.
Wada, I., and K. L. Wang (2009), Common depth of slab-mantle decoupling: Reconciling diversity and uniformity of subduction zones, *Geochem. Geophys. Geosyt.*, *10*, Q10009, doi:10.1029/2009GC002570.
Walowski, K. J., P. J. Wallace, E. H. Hauri, I. Wada, and M. A. Clynne (2015), Slab melting beneath the Cascade arc driven by dehydration of altered oceanic peridotite, *Nat. Geosci.*, *8*(5), 404–408.
Wang, K., and E. E. Davis (1992), Thermal effects of marine sedimentation in hydrothermally active areas, *Geophys J. Int.*, *110*(1), 70–78.
Weekly, R. T., W. S. D. Wilcock, D. R. Toomey, E. E. E. Hooft, and E. Kim (2014), Upper crustal seismic structure of the Endeavour segment, Juan de Fuca ridge from traveltime tomography: Implications for oceanic crustal accretion, *Geochem. Geophys. Geosyst.*, *15*, 1296–1315, doi:10.1002/2013GC005159.

Wilkens, R. H., G. J. Fryer, and J. Karsten (1991), Evolution of porosity and seismic structure of upper oceanic crust: Importance of aspect ratios, *J. Geophys. Res.*, *96*, 17,981–17,995, doi:10.1029/91JB01454.

Wilson, D. S. (1988), Tectonic history of the Juan de Fuca ridge over the last 40 million years, *J. Geophys. Res.*, *93*, 11,863–11,876, doi:10.1029/JB093iB10p11863.

Wilson, D. S. (1993), Confidence intervals for motion and deformation of the Juan de Fuca plate, *J. Geophys. Res.*, *98*, 16,053–16,071, doi:10.1029/93JB01227.

Wilson, D. S. (2002), The Juan de Fuca plate and slab—Isochron structure and Cenozoic plate motions, in *The Cascadia Subduction Zone and Related Subduction Systems. Seismic Structure, Intraslab Earthquakes and Processes, and Earthquake Hazards*, *U.S. Geol. Surv. Open-File Rep. 02-328*, edited by S. Kirby, K. Wang, and S. Dunlop, pp. 9–12, U.S. Geol. Surv., Menlo Park, Calif.

Wilson, D. S., D. A. Clague, N. H. Sleep, and J. L. Morton (1988), Implications of magma convection for the size and temperature of magma chambers at fast spreading ridges, *J. Geophys. Res.*, *93*, 11,974–11,984, doi:10.1029/JB093iB10p11974.